



Surface Roughness Analysis of 3D Printed Microchannels and Processing Characteristics of Abrasive Flow Finishing

Yongchao Jian^{1,2} · Yan Shi^{1,2} · Jia Liu^{1,2} · Cong Huang¹ · Zhi Guo^{1,2}

Received: 12 October 2020 / Accepted: 17 December 2020 / Published online: 9 March 2021
© King Fahd University of Petroleum & Minerals 2021

Abstract

Because of the low surface roughness of three-dimensional (3D) printed microchannels, in some environments, the use requirements cannot be met, and, at the same time, they are difficult to process. Therefore, a surface roughness analysis of 3D printed microchannels and post-processing using abrasive flow technology are proposed. The value of the inner surface roughness of the straight pipe part was calculated by using the least-squares method combined with the definite integral. Using the equal area principle, MATLAB curve fitting was used to numerically calculate the semicircular pipe section, and the relationship between the value of surface roughness and the bending radius of the scanning layer thickness is given. Use MATLAB image processing technology to study the processing area. The roughness of the inner wall of the pipeline was analyzed by laser confocal, stereo, and scanning electron microscopes. The results show that the roughness of the inner surface of the pipe increases with an increase in the thickness of the sweeping layer, an increase in the inclination angle, and a decrease in the radius of curvature. In the case of abrasive flow processing, the longer the processing time, the greater the grinding amount and the greater the amount of grinding outside the pipe wall in each one-way machining; further, the processing has obvious directionality.

Keywords 3D printing · Abrasive flow finishing · Surface roughness · Post processing · Matlab numerical calculation

1 Introduction

With the wide application of 3D technology in medical, automotive, aerospace, and other fields, post-processing technology for 3D printing components has attracted increasing attention, one aspect of which is the improvement of surface roughness [1–3]. Surface roughness and precision pose more difficult challenges for 3D printing than even the mechanical strength of 3D printed parts [4–6]. To improve the surface roughness after 3D printing, domestic and foreign scholars have conducted extensive research.

Ayrimis et al. [7] studied the effect of 3D printing parameters on roughness. Their results show that the thinner the

layer, the lower the roughness value. Song et al. [8] studied laser selection of molten Ti6Al4V alloy and Mumtaz et al. [9] studied the effect of laser selection of molten Inconel 625 powder on the roughness of the top and side of the sample. Their results show that higher frequency and lower scanning speed are beneficial to reducing the top roughness, and lower frequency and higher scanning speed are beneficial to improving the roughness of the side. Except for traditional machining, there is sparse research on post-processing of 3D printing surfaces. Bhaduri et al. [10] studied laser-polished 316L printed samples and studied the effects of different process parameters on polishing quality. Their results show that energy density and pulse overlap along the beam scanning direction were the most influential factors in improving surface quality. Zhang et al. [11] used electrochemical polishing to treat an Inconel 718 surface, improving the roughness of the outer surface of 3D printed parts by optimizing the processing time and temperature. Their experimental results show that adhesive particles begin to fall off after 1 min of processing, and a smooth surface appears after 4–5 min of processing. Atzeni et al. [12] studied the abrasive flow polishing process for additive manufacturing of aluminum

✉ Yan Shi
shiyan@cust.edu.cn

¹ School of Mechanical and Electric Engineering, Changchun University of Science and Technology, No.7089 Weixing Road, Changchun 130022, People's Republic of China

² National Base of International Science and Technology Cooperation for Optics, Changchun 130022, People's Republic of China



alloy plates. Unlmann et al. [13] studied the abrasive flow polishing process of additive manufacturing turbine blades. The results show that there is obvious unevenness in abrasive flow machining along the flow direction. Zhang et al. [14] studied the surface polishing technology of SLM workpiece with magnetic abrasive flow polishing technology. Singh et al. [15] used magnetic abrasive flow technology to study the surface polishing process of aluminum tubes. Williams et al. [16] performed abrasive flow polishing on additive manufacturing parts. The results show that it has a good improvement effect on the rough surface caused by the "step effect".

However, post-processing of the microchannel inside 3D printed metal material has not been reported. Based on this study, we propose post-processing of the inner wall of a 3D printed microchannel by using an abrasive flow technique. According to 3D printer theory, the formation mechanism of the surface roughness of the 3D printed sample is obtained, and the corresponding mathematical model is given. The roughness of the inner surface of the 3D printed sample was predicted, and then post-processing of the 316L printed microchannel was performed by using an abrasive flow technique to reduce the roughness of the inner surface.

2 Materials and Methods

2.1 Materials

For our 3D printing process, we used 316L metal powder with a particle size of 400 mesh. The specific ingredients are listed in Table 1. The abrasive flow polishing particles used were SiC particles with a density of 2975 kg/m^3 , a modulus of elasticity of 322 GPa, a Poisson's ratio of 0.142, and a

particle size of 600 mesh. The medium used was aviation hydraulic oil.

2.2 Test Equipment and Method

The 3D printing was done on a TruPrint3000 printer, delivering laser-selected melting with a layer thickness of $60 \mu\text{m}$ (which is about twice the diameter of the particles), at a laser power of 330 W and a scanning speed of 1000 mm/s. The scanning strategy was to scan from left to right layer by layer on a $5 \times 5 \text{ mm}$ checkerboard layer. The printing diagram is shown in Fig. 1.

The abrasive flow processing employed an environmentally friendly high-speed jet deburring machine at a working pressure of 5 MPa. Processing times of 10, 20, and 30 min were used for high-speed abrasive flow polishing of 3D printed samples. The grinding flow polishing diagram is shown in Fig. 2.

2.3 Analysis Method

The specific dimensions of the 3D printed sample are shown in Fig. 3. Figure 3 shows a schematic view of the specific dimensions of the 3D printed sample and the detailed position of the cutting section. The 3D printed sample processed by abrasive flow is cut by a wire-cutting machine from the A–A position. The cutting position A–A is 20 mm from the right end, which is the lowest end of the arc. At this time, the normal line of the circular section of the cutting section is just horizontal. The section after cutting is just a standard circle, and the cutting section is as shown on the right side of A–A. The cut workpiece is placed in an acetone solution and ultrasonically cleaned, and then sanded with sandpaper. The polished workpiece was photographed with a stereomicroscope on the cut section A–A after grinding, and the area

Table 1 Composition of 316L powder (wt%)

P	Cr	Ni	Mo	Mn	C	Si	Fe
<0.045	16.5–18.5	10.0–13.0	2–2.5	<2.0	<0.03	<0.015	Balance

Fig. 1 Diagram of 3D printing. **a** Actual diagram of 3D printing **b** schematic of 3D printing

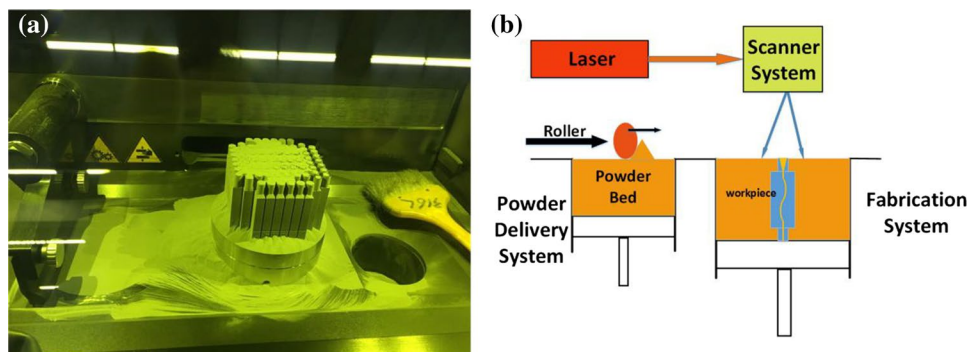


Fig. 2 Diagram of abrasive flow polishing. **a** Actual diagram of abrasive flow polishing **b** schematic of abrasive flow polishing

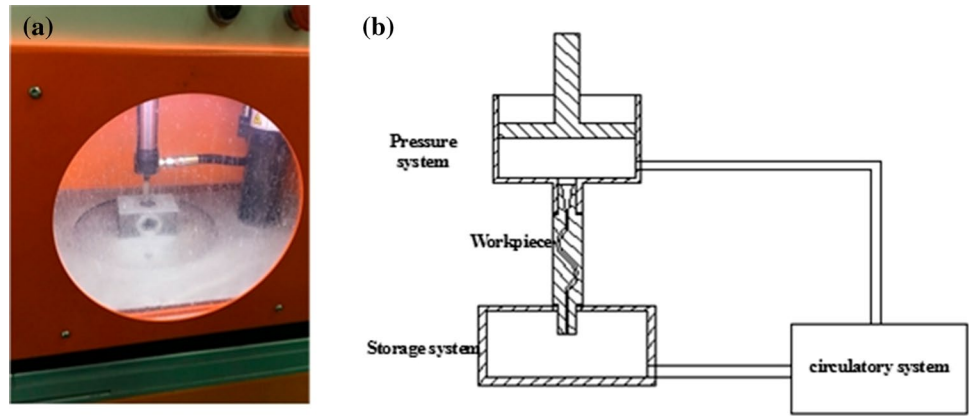


Fig. 3 Schematic of cutting position and cutting section

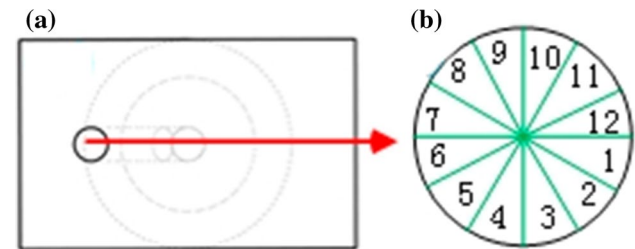
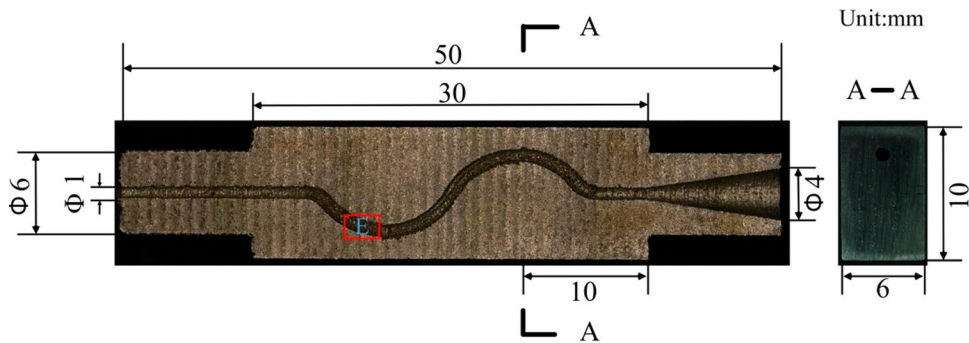


Fig. 4 **a** Schematic of a circular hole in the cutting section shooting direction. **b** 12-division diagram

of the circular hole was measured using the measuring tool of the stereomicroscope. The equivalent diameter was calculated to study the processing efficiency of the abrasive flow. The three-dimensional (3D) shape of the E region was extracted by a laser confocal microscope, and the roughness value of the bottom was calculated. Scanning electron microscopy was used to determine the microscopic morphology of the E region, and the change of the roughness of the tube wall after processing was observed. The unevenness of the inner and outer processing was then analyzed.

At the same time, the contour of the polished cutting section was extracted by using MATLAB, and the extracted contour was divided into 12 equal parts on the circumference according to the central angle. As shown in Fig. 3, the circular hole was divided into two parts. Figure 4a shows the

direction of the cut section, and Fig. 4b shows the 12-part division. The small fan-shaped area was calculated after aliquoting. By comparing the area of the fan-shaped area at the same position of the workpiece at different processing times, we could quantitatively analyze the position where the grinding process mainly occurs during the abrasive flow processing.

3 Analysis of Formation Mechanism of Inner Surface Roughness

3.1 Cause of Internal Surface Roughness

According to the actual design, formation of the roughness of the microchannel inner surface has two characteristics. One is produced by the step effect, such as Zones I and II, and the other is the adhesion caused by the partial melting of the unmelted powder at the wall surface after the input energy penetrates into the next layer, such as Zone III. As shown in Fig. 5, the rough surface of Zones I and II is mainly caused by the step effect, and the rough surface of Zone III is mainly caused by the dross. The main difference between Zones II and III is that, in the process of 3D printing, the 3D printed workpiece itself can be supported by the current printing layer. If the printed entity can be used as support for the current print layer, the inner surface roughness is

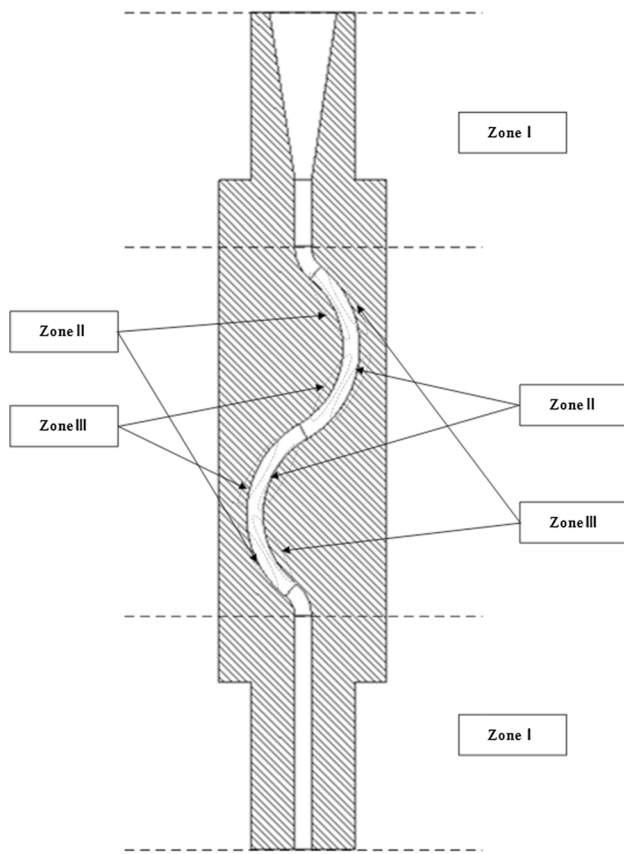
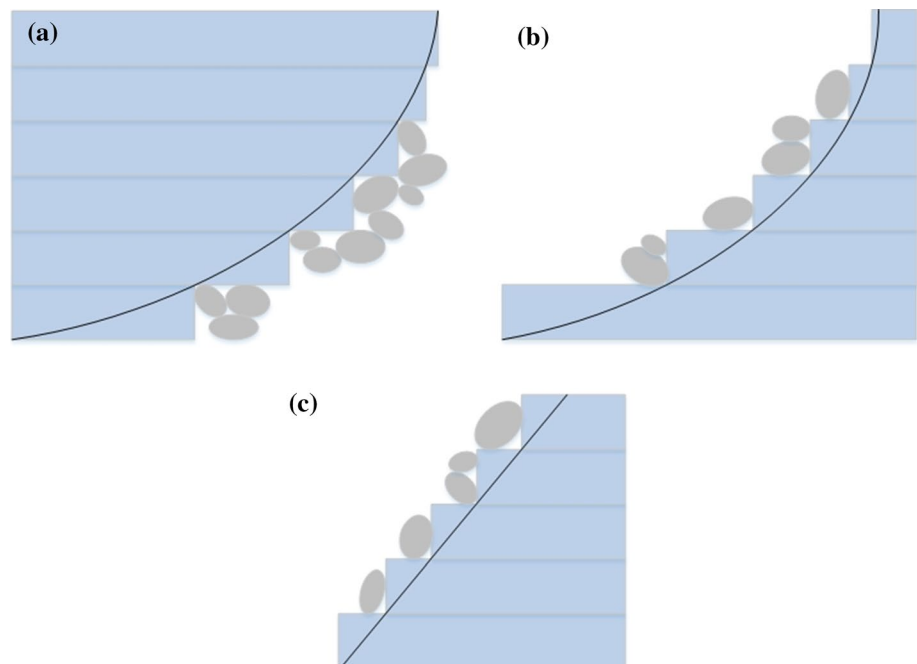


Fig. 5 Schematic of the overall surface roughness of the pipe in the microchannel

Fig. 6 Schematics of the formation of internal surface roughness of **a** slag hanging in Zone III, **b** the step effect in Zone II and **c** Zone I



mainly due to the step effect, such as Zone II. If the 3D printed workpiece itself cannot be supported as the current print layer, the inner surface roughness is mainly formed by “hanging slag,” such as Zone III.

In the case in which the printed entity cannot be used as a support, Zone III is mainly slag formed by adhesion. 3D printing is layered and the material is gradually printed. When printing the second layer, the input energy not only melts the current layer but also penetrates into the first layer to connect the two layers. It is the connection between the two layers that forms slag in Zone III; this is caused by the porous structure formed by the powder particles and the semimolten particles attached to the surface [9]. In the case in which the printed entity can be supported, Zones I and II are caused by the step effect. Each layer is scanned by scanning each slice and deposited on the inside and on the boundary. The entire part is formed in this way, thus forming a step effect [17–20]. Figure 6 shows the internal surface roughness. Figure 6a shows a schematic of the slag in Zone III, Fig. 6b shows a schematic of the step effect in Zone II, and Fig. 6c shows a schematic of the step in Zone I.

3.2 Analysis of the Step Effect in Part I of the Straight Pipe

In the case in which the printed entity cannot be supported, it is difficult to provide a corresponding mathematical model because of an increase in surface roughness caused by dross. Therefore, we mainly deduce the increase in surface roughness caused by the step effect in Zones I and III. The straight pipe portion and the curved pipe portion

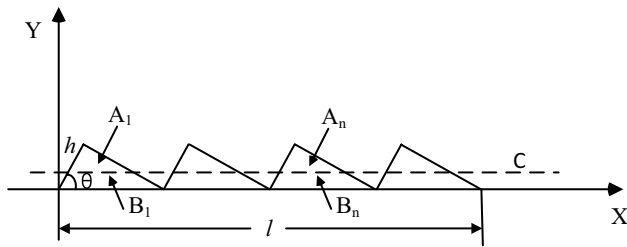


Fig. 7 Schematic of roughness calculation in Zone I

are essentially the same, except that their contour curves and mathematical expressions are different. To facilitate the mathematical calculation, only the step effect is considered, the slag and the step melting on the step are neglected, and the roughness forming model is appropriately simplified. A model capable of mathematical calculation is proposed and appropriately transformed.

Zone I is a straight pipe section, and its contour curve is a straight line. The roughness of the surface transformation in Zone I is shown in Fig. 7. C is the contour center line, which is the reference line for evaluating the surface roughness, and the shape of the contour centerline is the same as the ideal shape. *h* is the thickness of the sweeping layer, and θ is the tilt angle of the printing. To derive the mathematical expression for the roughness value of the Zone I region, the relationship between the roughness value of the straight tube portion of the 3D printing and the print layer thickness and the tilt angle is described. This will facilitate qualitative analysis of future actual production and provide a basis for the subsequent quantitative calculation.

We calculate the arithmetic contour centerline of Zone I using the equal area principle. Suppose there is a contour midline $y = c$. The contour of the step shape of the Zone I region is divided into upper and lower parts, and the specific expression for C can be calculated according to

$$A_1 + A_2 + \dots + A_n = B_1 + B_2 + \dots + B_n \tag{3.1}$$

The contour centerline C is calculated by bringing in the data:

$$C = \frac{2 - \sqrt{2}}{2} h \sin \theta \tag{3.2}$$

The arithmetic mean deviation from the point of the contour surface to the contour within the sampling length is calculated according to the following equation:

$$Ra = \frac{1}{l} \int_0^l |y(x) - c| dx \tag{3.3}$$

In Eq. (3.2), the arithmetic mean deviation of the contour is calculated using

$$Ra = \frac{2 - \sqrt{2}}{2} \frac{h \sin \theta}{\sin \theta + \cos \theta} = \frac{2 - \sqrt{2}}{2} h \frac{1}{1 + \frac{1}{\tan \theta}} \tag{3.4}$$

Equation (3.4) is derived and calculated according to the definition of surface roughness. It can be seen from Eq. (3.4) that the value of *Ra* increases as the scanning layer thickness and the tilt angle increase. Therefore, in 3D printing, the scanning layer thickness and the tilt angle can be appropriately reduced to reduce the surface roughness and increase the smoothness of the surface.

3.3 Step Effect Analysis of the Elbow Part of Zone II

The elbow portion of Zone II is formed by sweeping a part of the arc, so this contour midline $y = f(x)$ is part of the arc. The inner surface step effect is shown in Fig. 8. Figure 8a shows the actual step effect of the inner surface, and Fig. 8b shows a schematic of the step effect.

The step effect is transformed without considering the melting of the step and the small amount of dross near the step, which is convenient for mathematical calculation. Figure 9 shows a schematic of the roughness calculation.

The transformation diagram of Zone II is shown in Fig. 9a. Because the contour line is a curve, the amount of calculations is relatively large, so we used MATLAB for numerical calculation. Then, a plurality of sets of calculation data were used to fit a relationship between the roughness value *Ra* and the scanning layer thickness *h* and the radius of curvature *R*.

We created a graph, as shown in Fig. 9b, in MATLAB. The black line L1 is part of the arc curve, which is the contour of our design. The equation of the circle is $X^2 + Y^2 = R^2$. The red line is vertical and the length of each line is *h*. The blue line is horizontal; one section is perpendicular to the red line, and the other end intersects the arc curve at a point. The intersection point is the starting point of the next straight line, forming a step, and the step is numerically calculated for the subsequent contour extraction. We assume

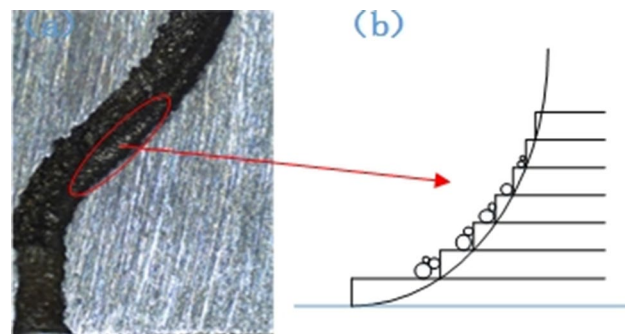
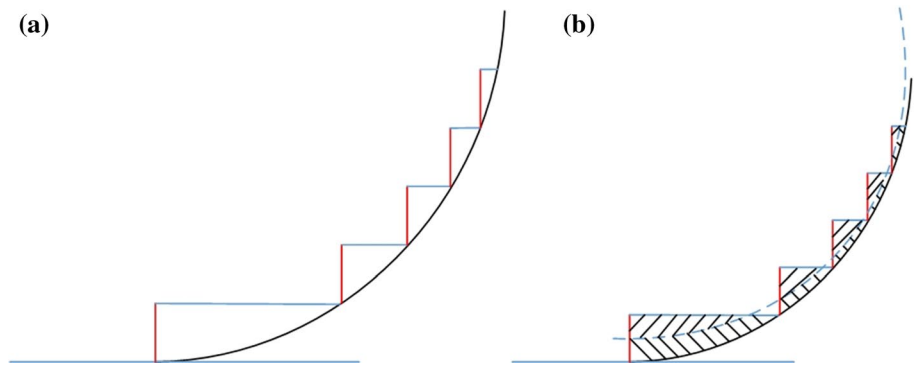


Fig. 8 Schematic of surface roughness formation in Zone II

Fig. 9 Schematics of **a** surface roughness conversion in Zone II and **b** contour curve extraction



that there is an arc curve L_3 passing through each step, entering from the vertical direction of each step, passing through the horizontal direction, and dividing the area included in the step into upper and lower parts. We then calculated the area of the two parts separately. When the areas are equal, L_3 (dashed line in the figure) is the contour curve. The point where the contour curve first passes through the step is the starting point, and the point that passes through the last step is the ending point, and the value of the roughness is calculated according to the following formula:

$$Ra = \frac{\int_{L_3} H ds}{S} \tag{3.5}$$

Therefore, each scanning layer thickness h and radius of curvature, R , correspond to a corresponding roughness value Ra . We calculated the corresponding roughness value Ra by giving multiple sets of scanning layer thickness h and radius of curvature, R . Consequently, a correspondence relationship between the set of roughness values Ra and the thickness h of the scanning layer and radius of curvature, R , can be obtained. After that, by using MATLAB drawing software, the corresponding image will appear, as shown in Fig. 10. According to the MATLAB calculation, the surface roughness of the circular tube increases with the increase in the thickness of the sweeping layer and the decrease in the radius of curvature, and the influence of the scanning layer thickness plays a major role.

4 Analysis of the Effect of Abrasive Flow Processing

Abrasive flow polishing is a technique for finishing the surface of a workpiece by colliding and rubbing the abrasive with a collective surface in a semisolid medium [21–24]. It improves surface roughness by removing a portion of the material by collision and friction between the abrasive particles and the surface of the substrate. The

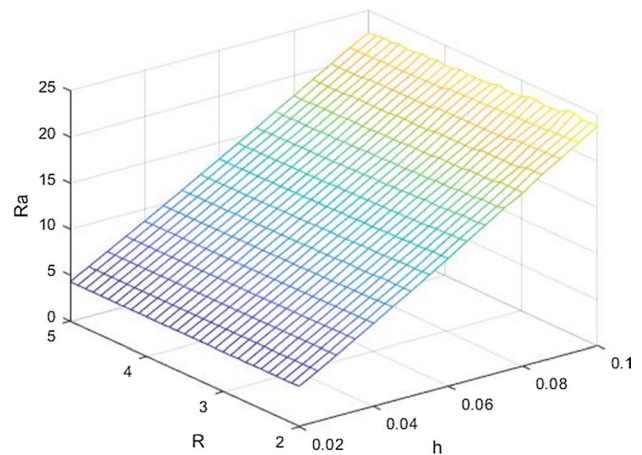


Fig. 10 Relationship between roughness and scanning layer thickness and radius of curvature

material removal mechanism mainly includes three deformation modes: elastic deformation, plastic deformation, and micro-cutting of materials [25]. Because of the good plasticity of the 316L powder molded parts, therefore, based on the micromachining theory of rigid metal erosion of Finnie [26], the wear law of particles on plastic materials under low-angle erosion is described accurately. The expression for the volume erosion rate is

$$v = K \frac{m_p v_p}{P_t} f(a) \tag{4.1}$$

with

$$f(a) = \begin{cases} \frac{1}{2} (\sin 2\alpha - 3 \sin^2 \alpha) & (0 < \alpha < \alpha_0) \\ \frac{1}{6} \cos^2 \alpha & (\alpha_0 < \alpha < 90^\circ) \end{cases} \tag{4.2}$$

where v is the volumetric erosion rate, K is the correction factor, m_p is the quality of the erosion particles, v_p is the velocity of particle impact, P_t is the flow stress of the material, n is the speed index, and α is the impact angle.

4.1 Analysis of the Processing Time Effect

By using abrasive flow equipment, 3D printed samples were processed for 10, 20, and 30 min, respectively, under a working pressure of 5 MPa. A cross-sectional view of the horizontal position of the curved section of the 3D printed sample was collected using a stereomicroscope in the E region, as shown in Fig. 11. Figure 11a shows the 3D print sample. Figures 11b and 12c, d show cross-sectional views when machining for 10, 20, and 30 min, respectively. Through the acquisition and measurement tools of the stereomicroscope, the base image of the cross-sectional circle of the 3D printed sample was collected, and the area of the cross-sectional circle was calculated in the E region.

The measurement results are plotted with the origin and the results are shown in Fig. 12. Figure 12 shows a histogram of the cross-sectional area of the cross section and the equivalent diameter for different processing times. It can be seen from the figure that, as processing time increases, the grinding amount increases gradually, the equivalent diameter and the cross-sectional area increase simultaneously, and the rate of increase gradually decreases. This indicates that, as processing time increases, the amount of grinding increases but at a lower rate of increase.

Measurement results of the roughness of the bottom of a 3D printed sample using a laser confocal microscope in the E region are shown in Fig. 13. Figure 13 shows the 3D top view of the bottom at different processing times. Figure 13(a) shows the 3D printed sample. Figure 13b–d

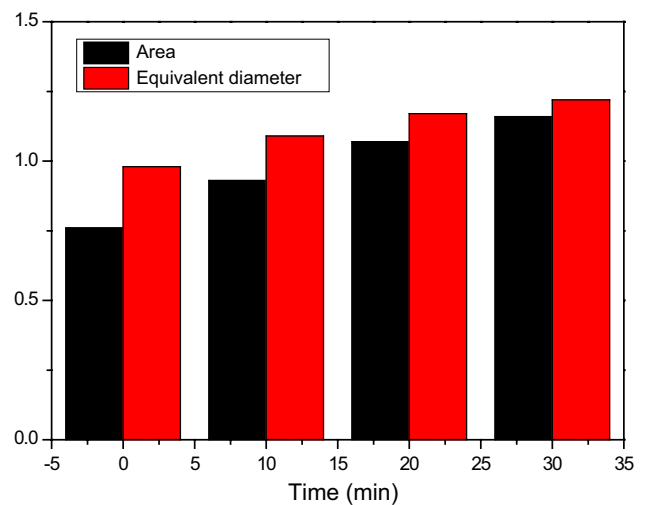


Fig. 12 Histogram of cross-sectional area and equivalent diameter

show the 3D topography at the bottom after 10, 20, and 30 min of processing, respectively. It can be seen from the 3D topography that, as the processing time increases, the roughness of the region D gradually decreases. When processing for 20 min, the transitions of the three regions, A, B, and C, are the most gradual, being uniform. Among them, when processing for 30 min, the B area is obviously the smallest, and there may be a scouring phenomenon with pits appearing locally.

Fig. 11 Circular area at different processing times. a 3D print sample. Areas at processing times of b 10 min, c 20 min, and d 30 min

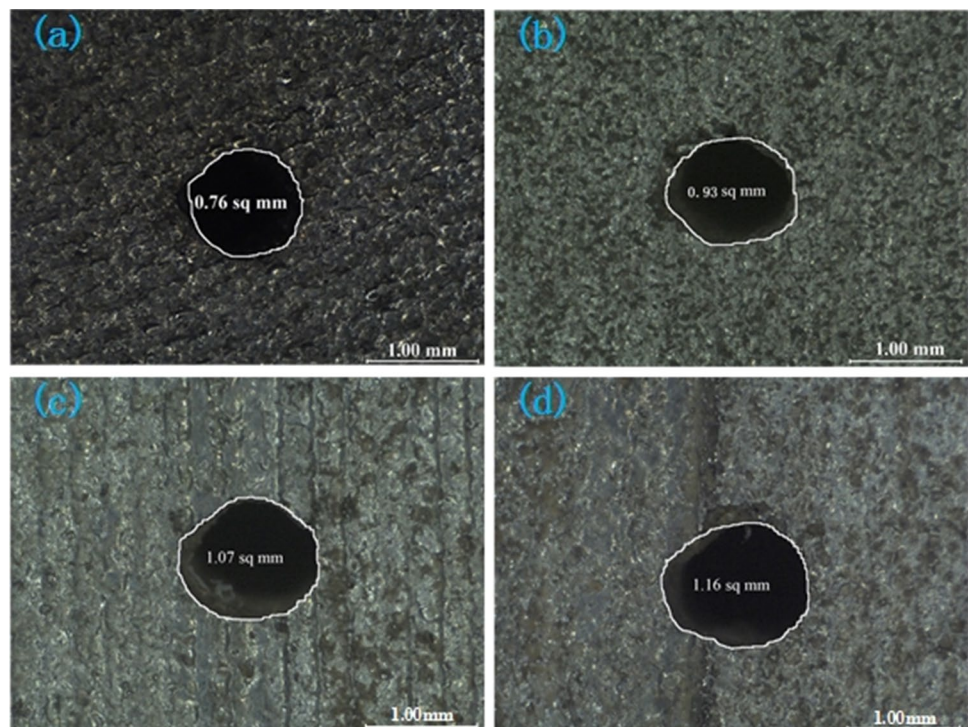


Fig. 13. 3D topography of the bottom of the workpiece at different processing times. **a** 3D printed sample. Topography for processing times of **b** 10 min, **c** 20 min, and **d** 30 min

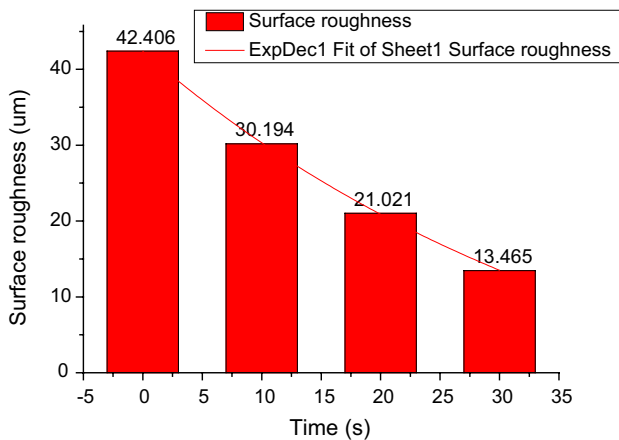
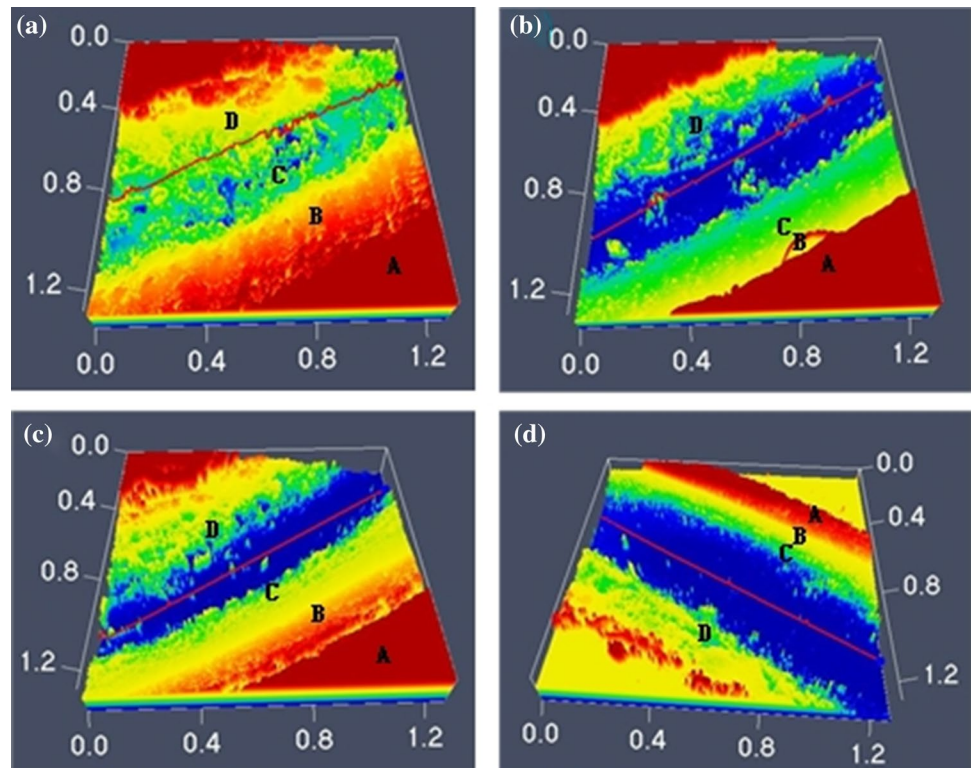


Fig. 14 Bottom roughness value

The roughness is measured at the red line position in the figure at the bottom of the 3D topography image taken by the laser confocal microscope. The roughness histogram is shown in Fig. 14, which shows the numerical value of the bottom roughness and the curve fitting using the ExpDec1 model. It can be seen from the figure and the fitted curve that, as the processing time increases, the value of the roughness gradually decreases, and the rate of decrease exhibits a downward trend, finally gradually approaching the critical surface roughness value. [27, 28] In other words, as

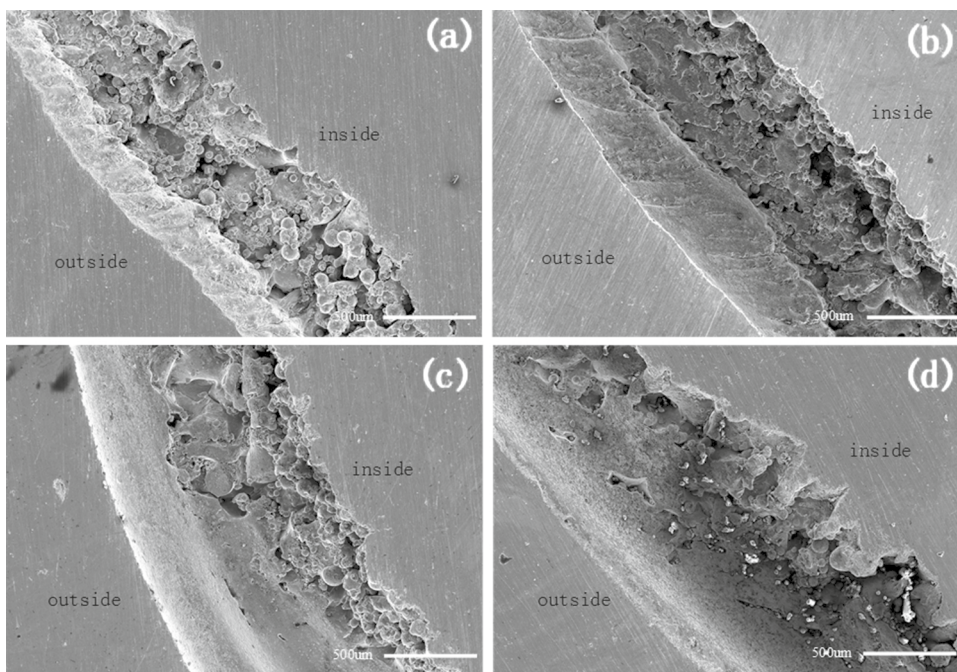
the processing time increases, the value of the roughness decreases, and finally it fluctuates within a small range.

The macroscopic morphology of the E region was photographed by scanning electron microscopy. The results at different processing times are shown in Fig. 15. Figure 15a shows the 3D printed sample. Figure 15b–d show scanning electron micrographs after processing times of 10, 20, and 30 min, respectively. It can be seen from the figure that the inner and outer sides of the processed areas exhibit different processing rules. Under the action of the centrifugal force of the curve, the processing is more intense on the outside, while the inner side is less processed, and the inner surface is still rough. As the processing time increases, the outer side gradually becomes smooth, but when the processing time reaches 30 min, the pits produced are processed, and the processing is excessive.

4.2 Analysis of the Grinding Position

To analyze the nonuniformity of cutting, we use MATLAB for image processing. The polished end face image taken by the stereomicroscope was imported into MATLAB for calculation. Noise is inevitably generated during image generation and transmission [29–31]. Consequently, we need to use filtering. We used Gauss filtering, in which the pixel values of each point in the image are calculated by a weighted average of nearby pixels. The Gauss calculation formula is

Fig. 15 Scanning electron micrographs of the E region at different processing times. **a** 3D print sample. Micrographs at processing times of **b** 10 min, **c** 20 min, and **d** 30 min



$$G(x, y) = \frac{1}{2\pi\sigma^2} e^{-\frac{(x^2+y^2)}{2\sigma}} \tag{4.3}$$

The Otsu algorithm is used for binarization. The basic idea is to assume a gray T value. The T value divides the gray level of the image into two groups. When the variance between the two groups is the largest, the gray level T is the optimal threshold of the image.

If the number of pixels in the image is N , the gray value range is $[0, L - 1]$, and the pixel corresponding to gray level i is n_i , then the probability is

$$P_i = n_i/N, \quad i = 0, 1, 2, \dots, L-1 \tag{4.4}$$

$$\sum_0^{L-1} P_i = 1 \tag{4.5}$$

We assume that the pixel values T in the image are divided into two categories, denoted as B_0 and B_1 . The gray value range of B_0 is $[0, T]$, and the gray value range of B_1 is $[T+1, L-1]$. The average value of the gray value of the image is then

$$u_T = \sum_0^{L-1} iP_i \tag{4.6}$$

Then the mean values of B_0 and B_1 are

$$u_0 = \sum_0^T iP_i/w_0 \quad u_1 = \sum_{T+1}^{L-1} iP_i/w_1 \tag{4.7}$$

where $w_0 = \sum_0^T P_i$ and $w_1 = \sum_{T+1}^{L-1} P_i = 1 - w_0$.

From the above formula,

$$u_T = u_0w_0 + u_1w_1 \tag{4.8}$$

The variance between classes is defined as

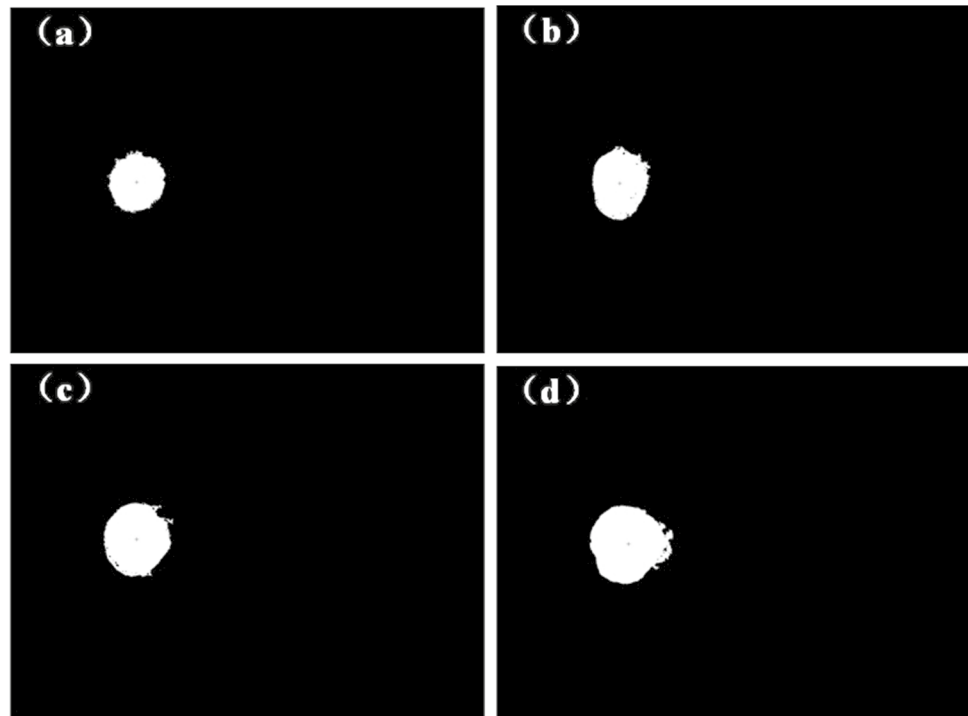
$$\delta^2 = w_0(u_0 - u_T)^2 + (u_1 - u_T)^2 \tag{4.9}$$

Let T take a value in the range $[0, L - 1]$. When the calculated value of T is the maximum, then the value of T is the optimal threshold calculated by the large law. Using the optimal threshold at this time, the image is binarized, and the processed circular hole area is extracted. Figure 16 shows the different processing time binarization maps. Figure 16a–d show binary diagrams after 0, 10, 20, and 30 min of processing, respectively.

The binarized image is divided into 12 segments counter-clockwise, with each small area of each aliquot having the same central angle, and these are sorted counterclockwise from the positive east. Figure 17 shows the 12-division areas at different processing time lengths. Figure 17a–d show sectional views of the position of the circular hole after processing for 0, 10, 20, and 30 min, respectively.

We calculated the number of pixels in each area, performed a conversion calculation, and calculated the area of each small area. We can then draw the area of each small area as a line chart, as shown in Fig. 18. From Fig. 18, it can be seen that, as the processing time increases, the area of the cut area generally exhibits an increasing trend. In each processing, the processing amount of area 4–9 is obviously

Fig. 16 Binarization diagrams after processing times of **a** 0 min, **b** 10 min, **c** 20 min, and **d** 30 min



greater than that in other areas, so it can be clearly seen that the grinding process takes place preferentially in area 4–9, and the processing exhibits obvious selectivity.

5 Conclusions

- (1) Through analysis of the 3D printing mechanism, about the complex workpiece, the roughness of the inner surface is summarized which is mainly divided into two types and three areas. If the printed entity can be used as support for the current print layer, the inner surface roughness is mainly due to the step effect and another is “hanging slag.” It can also explain the formation of all surface roughness in 3D printing. At the same time, through the theoretical calculation about Zone I and numerical calculation about Zone II, it will be provide the basis for the later theoretical analysis.
- (2) Through the theoretical calculation of the roughness value resulting from the inclination of the straight pipe, the surface roughness increases with the increase in the scanning layer and increase in the inclination angle. The roughness values of the bent portion calculated by MATLAB increase as the thickness of the scanning layer and the radius of curvature decrease.
- (3) When the inner pipe is treated by abrasive flow, the grinding process exhibits obvious directionality, with the grinding amount outside the pipe wall being significantly higher than that on the inner side of the pipe wall. At the same time, it is found that the processing effect is best when processing for 20 min, with longer times leading to obvious pits, which destroy the original pipe shape.



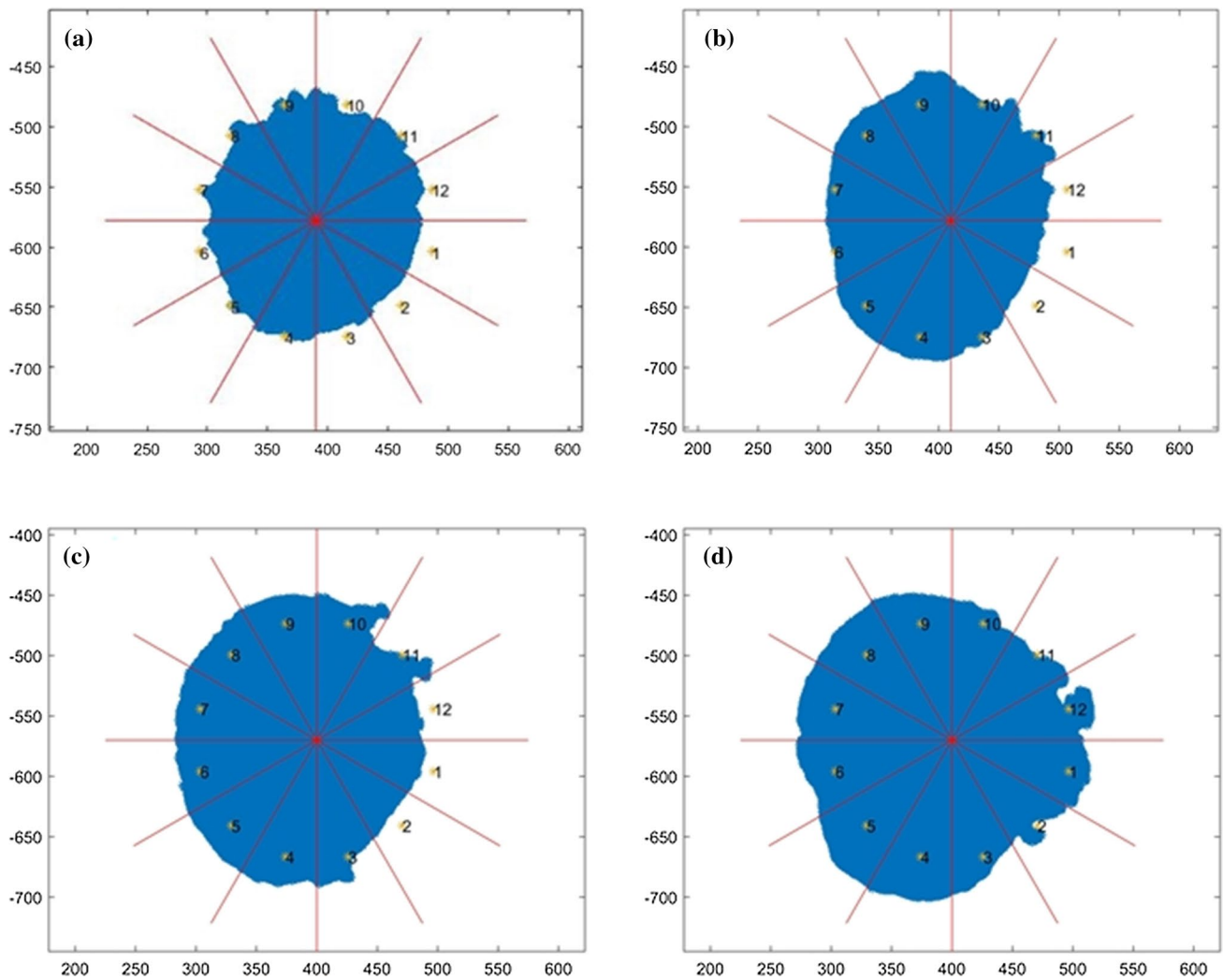


Fig. 17. 12-division areas at processing times a 0 min, b 10 min, c 20 min and d 30 min

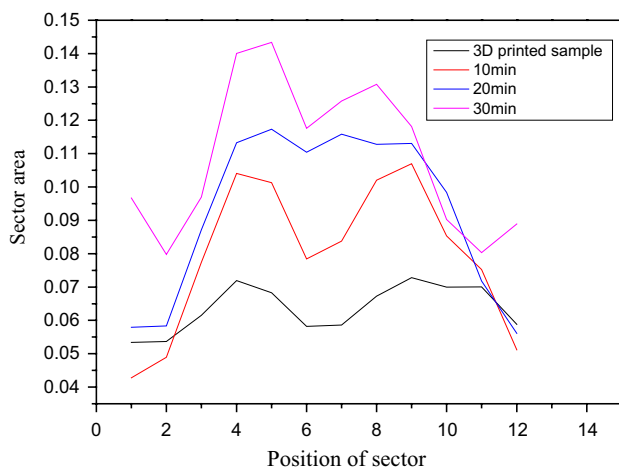


Fig. 18 Different areas of different processing times and area chart

Acknowledgements The authors are also grateful for the financial aids from the National key R&D Project (Grant No: 2017YFB1104601).

References

- Xu, C.; Dai, G.; Hong, Y.: Recent advances in high-strength and elastic hydrogels for 3D printing in biomedical applications. *Acta Biomater.* **95**, 50–59 (2019)
- Matta, A.K.; Kodali, S.P.; Ivvala, J.; Kumar, P.J.: Metal prototyping the future of automobile industry: a review. *Mater. Today: Proc.* **5**(9), 17597–17601 (2018)
- O’Hara, W.J.; Kish, J.M.; Werkheiser, M.J.: Turn-key use of an onboard 3D printer for international space station operations. *Addit. Manuf.* **24**, 560–565 (2018)
- Kruth, J.P.; Leu, M.C.; Nakagawa, T.: Progress in additive manufacturing and rapid prototyping. *CIRP Ann. Manuf. Technol.* **47**(2), 525–540 (1998)
- Wohlers, T.: Future potential of rapid prototyping and manufacturing around the world. *Rapid Prototyp. J.* **1**(1), 4–10 (1995)

6. Lalehpour, A.; Janeteas, C.; Barari, A.: Surface roughness of FDM parts after post-processing with acetone vapor bath smoothing process. *Int. J. Adv. Manuf. Technol.* **95**, 1505–1520 (2017)
7. Ayrlimis, N.: Effect of layer thickness on surface properties of 3D printed materials produced from wood flour/PLA filament. *Polym. Test.* **71**, 163–166 (2018)
8. Song, B.; Dong, S.; Zhang, B., et al.: Effects of processing parameters on microstructure and mechanical property of selective laser melted Ti6Al4V. *Mater. Des.* **35**, 120–125 (2012)
9. Mumtaz, K.; Hopkinson, N.: Top surface and side roughness of Inconel 625 parts processed using selective laser melting. *Rapid Prototyp. J.* **15**(2), 96–103 (2009)
10. Bhaduri, D.; Penchev, P.; Batal, A., et al.: Laser polishing of 3D printed mesoscale components. *Appl. Surf. Sci.* **405**, 29–46 (2017)
11. Zhang, B.; Xiaohua, L.; Bai, J., et al.: Study of selective laser melting (SLM) Inconel 718 part surface improvement by electrochemical polishing. *Mater. Des.* **116**, 531–537 (2017)
12. Atzeni, E.; Barletta, M.; Calignano, F.: Abrasive fluidized bed (AFB) finishing of AISi10Mg substrates manufactured by direct metal laser sintering (DMLS). *Addit. Manuf.* **10**, 15–23 (2016)
13. Uhlmann, E.; Schmiedel, C.; Wendler, J.: CFD Simulation of the abrasive flow machining process. *Proc. Cirp* **31**, 209–214 (2015)
14. Zhang, J.; Chaudhari, A.; Wang, H.: Surface quality and material removal in magnetic abrasive finishing of selective laser melted 316L stainless steel. *J. Manuf. Process.* **45**(Sep), 710–719 (2019)
15. Singh, P.; Singh, L.; Sehijpal, S.: Manufacturing and performance analysis of mechanically alloyed magnetic abrasives for magneto abrasive flow finishing. *J. Manuf. Process.* **50**, 161–169 (2020)
16. Williams, R.E.; Melton, V.L.: Abrasive flow finishing of stereolithography prototypes. *Rapid Prototyp. J.* **4**(2), 56–67 (1998)
17. Pandey, P.M.; Reddy, N.V.; Dhande, S.G.: Improvement of surface finish by staircase machining in fused deposition modeling. *J. Mater. Process. Technol.* **132**(1–3), 323–331 (2003)
18. Pandey, P.M.; Reddy, N.V.; Dhande, S.G.: Real time adaptive slicing for fused deposition modelling. *Int. J. Mach. Tools Manuf.* **43**(1), 61–71 (2003)
19. Thrimurthulu, K.; Pandey, P.M.; Reddy, N.V.: Optimum part deposition orientation in fused deposition modeling. *Int. J. Mach. Tools Manuf.* **44**(6), 585–594 (2004)
20. Boschetto, A.; Bottini, L.: Surface improvement of fused deposition modeling parts by barrel finishing. *Rapid Prototyp. J.* **21**(6), 686–696 (2015)
21. Jain, R.K.; Jain, V.K.: Stochastic simulation of active grain density in abrasive flow machining. *J. Mater. Process. Technol.* **152**(1), 17–22 (2003)
22. Gorana, V.K.; Jain, V.K.; Lal, G.K.: Experimental investigation into cutting forces and active grain density during abrasive flow machining. *Int. J. Mach. Tools Manuf.* **44**(2), 201–211 (2003)
23. Gorana, V.K.; Jain, V.K.; Lal, G.K.: Forces prediction during material deformation in abrasive flow machining. *Wear* **260**(1), 128–139 (2004)
24. Jain, R.K.; Jain, V.K.: Specific energy and temperature determination in abrasive flow machining process. *Int. J. Mach. Tools Manuf.* **41**(12), 1689–1704 (2001)
25. Kumar, S.S.; Hiremath, S.S.: A review on abrasive flow machining (AFM). *Proc. Technol.* **25**, 1297–1304 (2016)
26. Finnie, I.: Some observations on the erosion of ductile metals. *Wear* **19**(1), 81–90 (1972)
27. Jain, V.K.: Magnetic field assisted abrasive based micro-/nano-finishing. *J. Mater. Process. Tech.* **209**(20), 6022–6038 (2009)
28. Jayswal, S.C.; Jain, V.K.; Dixit, P.M.: Modeling and simulation of magnetic abrasive finishing process. *Int. J. Adv. Manuf. Technol.* **26**(5–6), 477–490 (2005)
29. Khitun, A.; Bao, M.; Wang, K.L.: Magnetic cellular nonlinear network with spin wave bus for image processing. *Superlattices Microstruct.* **47**(3), 464–483 (2010)
30. Mora, C.; Kwan, A.: Sphericity, shape factor, and convexity measurement of coarse aggregate for concrete using digital image processing. *Cem. Concr. Res.* **30**(3), 351–358 (2000)
31. Szmaja, W.: Digital image processing system for magnetic domain observation in SEM. *J. Magn. Mater.* **189**(3), 353–365 (1998)

